

Geometry and elasticity of strips and flowers

M. Marder

*Center for Nonlinear Dynamics and Department of Physics The University of Texas at Austin, Austin TX 78712, USA**

N. Papanicolaou

Department of Physics, University of Crete, and Research Center of Crete, Heraklion, Greece[†]

We solve several problems that involve imposing metrics on surfaces. The problem of a strip with a linear metric gradient is formulated in terms of a Lagrangean similar to those used for spin systems. We are able to show that the low energy state of long strips is a twisted helical state like a telephone cord. We then extend the techniques used in this solution to two-dimensional sheets with more general metrics. We find evolution equations and show that when they are not singular, a surface is determined by knowledge of its metric, and the shape of the surface along one line. Finally, we provide numerical evidence that once these evolution equations become singular, either the surface is not differentiable, or else the metric deviates from the target metric as a result of minimization of a suitable energy functional.

PACS numbers: 45.70.Qj, 02.40.-k

I. INTRODUCTION

In a series of experiments performed in 2002, Sharon *et al.*[1] showed that thin sheets deformed in a smooth fashion spontaneously fold into convoluted shapes with much less symmetry than the original deformation. These experiments raised many questions about the relationship between local changes in distance within a sheet, and the global shape the sheet adopts. The first theoretical papers that set about explaining the experiments[2, 3, 4, 5, 6] established certain points, but left many others unsettled. What was most clearly established was that one should study the problem by choosing a metric function suggested by the physical process that deformed the sheet, and trying to determine what surfaces were compatible with this metric. Much of the effort in these papers was devoted to exploring the problem of a long thin strip of material with a linear metric gradient in one direction. This strip problem was not solved in great generality, and its relation to the more general two-dimensional problems was not definite. Furthermore, the basic idea of the calculations was not clear. On the one hand, the papers spoke of imposing a metric on a sheet, while on the other there were many indications that the actual metric of the final shape adopted by the sheet was something else.

This paper has three main sections which address the questions we have just described.

First, we return to the problem of the long strip with a metric gradient and provide a more complete solution than was afforded previously. In particular, we find the lowest-energy shape of this strip when it becomes very long. In this limit, the strip coils into a helix like a telephone cord. The edge of a flower or a leaf cannot behave in this way. Therefore, solutions of the strip problem have only limited relevance to the more general two-dimensional questions raised by the experiments. However, the formal techniques used to solve the strip

prove to be helpful, and provide the basis for our approach to the two-dimensional problem.

Second, we return to the problem of two-dimensional sheets, and attempt to determine the extent to which specifying a metric determines the surface. We can discard the possibility that a metric alone can dictate the shape of a surface. For example, a piece of paper can be bent into infinitely many smooth shapes, all of which share the same Euclidean metric. This property is not simply due to the fact that the piece of paper is initially flat. Tape the paper into the shape of a cylinder, and still it can be deformed in infinitely many ways without change of metric. A classic theorem of differential geometry states that surfaces are uniquely determined, up to rotations and translations, by the metric, and by the second fundamental form, provided that they satisfy the Gauss-Codazzi equations[7]. However, the second fundamental form provides more information than is needed. We will show that if one knows the metric of a surface, and the shape of the surface along one line, then the rest of the surface is determined by an evolution equation. This statement must be qualified. The procedure that determines the surface typically contains singularities, and the attempt to find the surface with geometry alone comes to a halt.

Third, we discuss numerical procedures to find surfaces corresponding to metrics for which the evolution equations of the previous section become singular. We describe in some detail an energy functional whose minima should provide surfaces that approach a desired target metric as closely as possible. In cases where evolution equations dictate surfaces based upon geometry alone, the energy functional recovers them. When the evolution equations fail to find a surface, then either the energy functional finds a non-differentiable surface, or else it finds a smooth flower-like surface whose metric is different from the one that was supposedly imposed.

II. GROUND STATE FOR TWISTED STRIPS

Reference [8] shows a number of thin strips cut from the edge of a leaf. Each of them curls up into a circle, with the

*Electronic address: marder@chaos.ph.utexas.edu

[†]Electronic address: papanico@physics.uoc.gr

curvature of each strip depending upon the gradient of the metric at that point in the leaf. Such observations suggested that the rippling pattern at the edge of a leaf could be understood by focusing upon a thin strip of material with a metric gradient. Such a strip, freely allowed to seek out its lowest energy state simply curls up into a circle. Therefore, the additional constraint was added that the two ends of the strip had to be some distance λ apart[2]. This problem yielded non-trivial solutions[2, 3, 5, 6]. Certain special cases could be found analytically. Somewhat more general solutions could be found numerically. However, the numerical procedures were not very stable, and left open a number of questions. For example, there was some speculation that as the length L of the curved strip became infinite with L/λ kept finite, the lowest-energy state might be fractal. This speculation was incorrect, as we now show through a correct solution of the problem.

A. Problem setting

We briefly review the specification of the strip problem. Consider a circular strip of paper, as shown in Figure 1, of radius R , length $L = 2\pi R$, width w , and thickness t . The length L can be arbitrary, and may be greater or less than $2\pi R$. We will be interested in strips where the following limits apply:

$$\left(\frac{w}{R}\right)^2 \ll \frac{t}{R} \ll \frac{w}{R} \ll \frac{L}{R}. \quad (1)$$

When these conditions hold, the energy of the strip takes a very simple form as a functional of a line passing through the center of the strip[2].

In particular, let s be the arc length along the center of the strip. The low-energy conformations of the strip are captured by two orthonormal vectors $\hat{r}_1(s)$ and $\hat{r}_2(s)$, where \hat{r}_1 points along the arc s , and \hat{r}_2 lies in the plane of the strip and is orthogonal to \hat{r}_1 . Define also $\hat{r}_3 = \hat{r}_1 \times \hat{r}_2$, so as to obtain a set of unit vectors that describes in a natural way the local orientation of the strip. The location $\vec{r}(s)$ of each point along the center-line of the strip can be obtained from

$$\vec{r}(s) = \int_0^s ds' \hat{r}_1(s'). \quad (2)$$

At each point s' along the way, the precise orientation of the strip is specified by the unit vector \hat{r}_2 , or equivalently by the unit vector \hat{r}_3 , which is normal to the strip. Therefore, the vectors $\hat{r}_1(s)$ and $\hat{r}_2(s)$ contain all the information necessary to deduce the shape of the strip when it is embedded in three-dimensional space. The inequalities (1) ensure that the strip remains essentially flat and featureless in the direction pointing along \hat{r}_2 .

In terms of the vectors $\hat{r}_1(s)$ and $\hat{r}_2(s)$ the energy of the strip is given by[2, 3]

$$U = \int_0^L ds \mathcal{E}(s), \quad (3)$$

where

$$\mathcal{E} = \frac{C_1}{2} (|\hat{r}_1'|^2 - 1/R^2) + \frac{C_2}{2} (|\hat{r}_2'|^2 - 1/R^2), \quad (4)$$

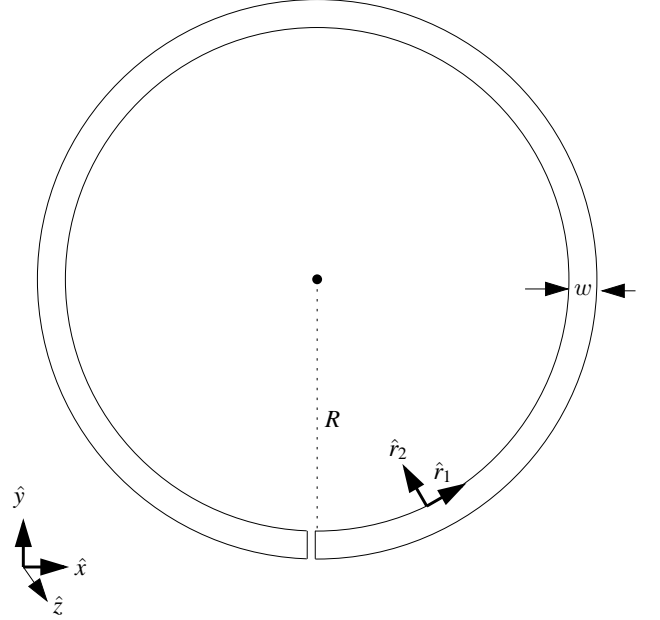


FIG. 1: The buckled strips studied in this section can be examined by cutting out this circular strip, of radius R and width w . Roughly speaking, the main question addressed here is to predict the shape of the strip when the two ends are pulled apart to some specified distance and relative orientation. For the general solutions studied in this section, the total length L of the strip need not equal $2\pi R$.

and primes indicate derivatives with respect to arc length s .

This energy is subject to two constraints. The first is a *local constraint* that results from the fact that the strip has a metric gradient in the direction of \hat{r}_2 that causes it to want to curl up with radius of curvature R . This constraint is captured by the condition

$$\hat{r}_1' \cdot \hat{r}_2 = -\hat{r}_2' \cdot \hat{r}_1 = 1/R. \quad (5)$$

The second constraint is that the ends of the strip be pulled apart by some distance; this constraint prevents the strip from simply curling up into a circle. We impose this constraint through

$$(\vec{r}(L) - \vec{r}(0)) \cdot \hat{z} = \lambda. \quad (6)$$

That is, the z component of the difference between starting and ending points of the strip is constrained to have value λ . By scanning through values of λ , one equivalently scans through all allowed distances between the starting and ending point of the strip. The constraint in the form of Eq. (6) is much easier to work with formally than if it were literally expressed in terms of end-to-end distance. For definiteness, we choose a fixed (laboratory) frame as shown in Figure 1. The \hat{z} axis is taken to be perpendicular to the plane defined by the initial (undeformed) circular strip, while the \hat{x} and \hat{y} axes point along the initial directions of \hat{r}_1 and \hat{r}_2 at one of the endpoints of the strip.

The trihedral $\hat{r}_1, \hat{r}_2, \hat{r}_3$ uses nine coordinates to represent the orientation of the strip, when in fact only three are needed.

Further analysis is greatly simplified by rewriting the unit vectors in terms of Euler angles (Ref.[9] Eq.4.46), through

$$\begin{aligned}\hat{r}_1 &= [\cos \psi \cos \phi - \cos \theta \sin \phi \sin \psi, \cos \psi \sin \phi + \cos \theta \cos \phi \sin \psi, \sin \theta \sin \psi]; \\ \hat{r}_2 &= [-\sin \psi \cos \phi - \cos \theta \sin \phi \cos \psi, -\sin \psi \sin \phi + \cos \theta \cos \phi \cos \psi, \sin \theta \cos \psi]; \\ \hat{r}_3 &= [\sin \theta \sin \phi, -\sin \theta \cos \phi, \cos \theta].\end{aligned}\quad (7)$$

With this representation, we can rewrite the local constraint Eq. (5) as

$$\cos \theta \phi' + \psi' = 1/R; \quad (8)$$

again, primes refer to derivatives with respect to the arc length s .

Writing out Eq. (4) in terms of the Euler angles one has

$$\begin{aligned}\mathcal{E} &= \frac{1}{2} [(C_2 - C_1) \cos^2 \psi + C_1] \theta'^2 \\ &+ (C_2 - C_1) \cos \psi \sin \psi \sin \theta \phi' \theta' \\ &+ \frac{1}{2} [(C_1 - C_2) \cos^2 \psi + C_2] \sin^2 \theta \phi'^2.\end{aligned}\quad (9)$$

In order to impose the global constraint Eq. (6), we will employ a Lagrange multiplier, and write down the Lagrangean

$$\begin{aligned}\mathcal{L} &= \frac{1}{2} [(C_2 - C_1) \cos^2 \psi + C_1] \theta'^2 \\ &+ (C_2 - C_1) \cos \psi \sin \psi \sin \theta \phi' \theta' \\ &+ \frac{1}{2} [(C_1 - C_2) \cos^2 \psi + C_2] \sin^2 \theta \phi'^2 \\ &- h \sin \psi \sin \theta.\end{aligned}\quad (10)$$

Note that ϕ' appears in Eq. (10), but not ϕ itself. This fact will allow for further simplification.

The constants C_1 and C_2 depend upon elastic properties of the strip. For a particular case studied in Ref.[5], they are related through $2C_2 = 3C_1$. Materials with different elastic properties would give different constants, so we take C_1 and C_2 as free variables. The structure of the equations is particularly simple when $C_1 = C_2$, so we will begin with that case, and return later to the more general situation.

Adopting $C_1 = C_2 = 1$, the Lagrangean of Eq. (10) simplifies to

$$\mathcal{L} = \frac{1}{2} \theta'^2 + \frac{1}{2} \phi'^2 \sin^2 \theta - h \sin \psi \sin \theta. \quad (11)$$

All appearances of ϕ can now be eliminated by employing the local constraint Eq. (8) to give

$$\mathcal{L} = \frac{1}{2} \theta'^2 + \frac{1}{2} (\psi' - 1/R)^2 \tan^2 \theta - h \sin \psi \sin \theta. \quad (12)$$

Similar Lagrangeans appear in the study of spin systems[10]. The equations of motion following from Eq. (12) are

$$\left[(\psi' - 1/R) \tan^2 \theta \right]' = -h \cos \psi \sin \theta \quad (13a)$$

$$\theta'' = (\psi' - 1/R)^2 \frac{\sin \theta}{\cos^3 \theta} - h \sin \psi \cos \theta \quad (13b)$$

B. Particular solution

Ref. [2] provided a family of exact solutions, and we search for these again with this new formalism. We find that they emerge if one sets $h = 0$ in Eqs. (13). In this case, one immediately integrates Eq. (13a) to obtain

$$(\psi' - 1/R) \tan^2 \theta = \beta, \quad (14)$$

where β is an integration constant. Inserting this relation into Eq. (13b) and integrating gives

$$\begin{aligned}\theta' &= \sqrt{\alpha^2 - \beta^2 / \sin^2 \theta} \\ \Rightarrow \cos \theta &= -\sqrt{1 - (\beta/\alpha)^2} \sin(\alpha s),\end{aligned}\quad (15)$$

where α is an additional integration constant. Without loss of generality one can choose $\alpha > 0$. Note from Eq. (15) that $\alpha > \beta$ if the solutions are to remain real.

For ψ one obtains

$$\psi = \tan^{-1} \left((\beta/\alpha) \tan(\alpha s) \right) - (\beta - 1/R)s + \psi_0. \quad (16)$$

Similarly, for ϕ one obtains

$$\phi = -\tan^{-1} \left(\sqrt{(\alpha/\beta)^2 - 1} \cos(\alpha s) \right) + \phi_0; \quad (17)$$

the integration constants ψ_0 and ϕ_0 give the value of ψ and ϕ when $s = 0$.

The global constraint Eq. (6) requires that

$$\int_0^L ds \sin \theta \sin \psi = \lambda. \quad (18)$$

As λ becomes large, it is only possible to satisfy Eq. (18) if $\sin \theta$ and $\sin \psi$ have the same period. Comparing Eqs. (16) and (15), one sees that this condition can be satisfied by taking

$$\beta = \alpha + 1/R. \quad (19)$$

With this choice, one has

$$\sin \theta \sin \psi = \hat{r}_1 \cdot \hat{z} = (\alpha R + \sin^2(\alpha s))/(\alpha R), \quad (20)$$

which with a bit of manipulation upon setting $R = 1$ reproduces Eq. (41a) in Ref. [2]; note that the x axis in that reference corresponds to the z axis here. The remainder of the special solution obtained previously can be recovered as well. Since this special solution depends upon setting $h = 0$, or equivalently to fixing a relationship between λ and L not required by the original problem, we move to a numerical approach capable of solving the problem in greater generality.

C. Numerical solutions

We can obtain reliable numerical ground states of Eq. (11) by changing the form of the Lagrange multiplier to enforce the global constraint in a fashion that involves a positive definite functional:

$$F = \int_0^L ds \left[\frac{1}{2} \theta'^2 + \frac{1}{2} (\psi' - 1/R)^2 \tan^2 \theta \right] + H \left(\lambda - \int_0^L ds \sin \psi \sin \theta \right)^2, \quad (21)$$

where H is chosen on the order of 100. To find solutions, we simply minimize F .

In the minimization procedure we fix boundary conditions on θ and ψ at $s = 0$ and $s = L$. We may also choose the initial ($s = 0$) value of ϕ , but its final ($s = L$) value is left free to adjust according to Eq. (8). Now we keep one of the endpoints of the strip fixed and orient corresponding initial directions of \hat{r}_1 and \hat{r}_2 along the \hat{x} and \hat{y} axes of the laboratory frame. Noting that when $\theta = 0$, the orientation of the trihedral depends only upon $\phi + \psi$, the initial values of the Euler angles are set at

$$\theta(0) = 0, \quad \psi(0) + \phi(0) = 0. \quad (22)$$

At the other endpoint, the values of θ and ψ are chosen arbitrarily; e.g.,

$$\theta(L) = \pi/3, \quad \psi(L) = \pi/4, \quad (23)$$

while the end-to-end distance is controlled by the parameter λ . A numerical solution for $L = 13$ and $\lambda = 0.75L$ yields values for θ and ψ shown in Figure 2. The angle $\phi = \phi(s)$ is

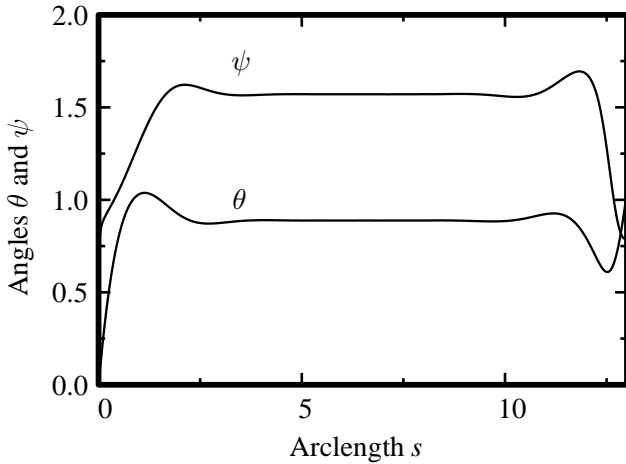


FIG. 2: Plot of Euler angles θ and ϕ for system with total length $L = 13$, constrained to have height in \hat{z} direction $\lambda = .75L$. Note that apart from some variation near the endpoints needed to obey the boundary conditions, both angles go to constant values throughout most of the length of the sample.

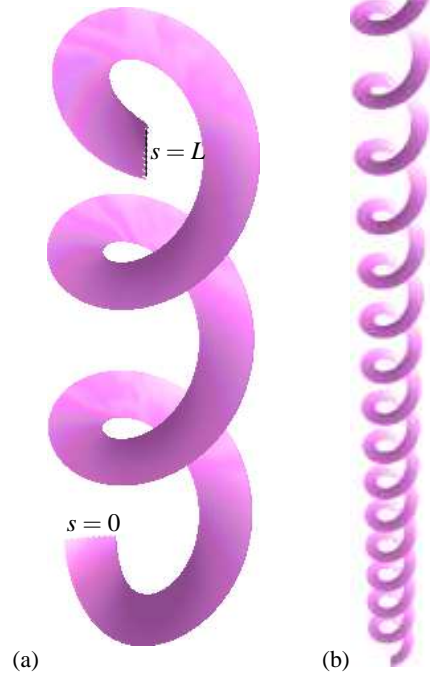


FIG. 3: (a) Three-dimensional visualization of solution shown in Figure 2 (in color). (b) Visualization of low-energy solution for a long strip with $\lambda/L = 0.625$. The strip winds in helical fashion around the \hat{z} axis (in color).

obtained by an elementary integration of Eq. (8), and the complete orthonormal trihedral from Eq. (7). It is then straightforward to calculate $\vec{r} = \vec{r}(s)$ from Eq. (2) which determines the relative position of the strip in three-dimensional space, as illustrated in Figure 3 (a).

One property of the solution that might seem unsatisfactory is that the strip wraps a number of times around the \hat{z} axis. If one were to grab two ends of a strip and pull them apart, this would not be allowed. If one wants to find energy-minimizing solutions without any net twist around the vertical axis, the following strategy is effective: Take a solution obeying the boundary conditions

$$\theta(L) = \pi/2, \quad \psi(L) = \pi/2, \quad (24)$$

produce a mirror image with $z \rightarrow -z, x \rightarrow x, y \rightarrow y$. The resulting function also minimizes the functional F . It can be glued on to the solution found so far, joining smoothly to it at $s = L$ because of Eq. (24), and will continue on to terminate at $(0, 0, 2\lambda)$ when $s = 2L$. The second half of the solution reverses the twist produced by the first half. In all cases we have checked, solutions of this type are the lowest-energy solutions without net twist.

A notable feature of Figure 2 and others like it is that the angles θ and ψ quickly approach constant values away from the endpoints, which do not depend on the specific boundary conditions (22) and (23). Thus we conclude that for *long strips*, the energy minimizing solutions have the following properties: θ and ψ are constants such that

$$\sin \psi \sin \theta = \lambda/L, \quad (25)$$

in order to satisfy the global constraint. According to Eq. (13a), $\cos \psi \sin \theta = 0$, which is compatible with Eq. (25) only if

$$\psi = \pi/2, \quad \sin \theta = \lambda/L. \quad (26)$$

For solutions obeying Eq. (18), the corresponding energy density

$$\mathcal{E} = \frac{1}{2R^2} \tan^2 \theta = \frac{1}{2R^2} \frac{\lambda^2}{L^2 - \lambda^2} \quad (27)$$

is also constant, independent of s . Nevertheless, the solution oscillates because of Eq. (8), which implies that

$$\phi = \frac{s}{R \cos \theta} = \frac{s}{R \sqrt{1 - (\lambda/L)^2}}. \quad (28)$$

The period of oscillation is given by

$$s_{\text{osc}} = 2\pi R \cos \theta = 2\pi R \sqrt{1 - (\lambda/L)^2}. \quad (29)$$

and the distance the solution travels when s traverses this arc-length is

$$z_{\text{osc}} = 2\pi R \sin \theta \cos \theta = 2\pi R \sqrt{1 - (\lambda/L)^2} \frac{\lambda}{L}. \quad (30)$$

This last expression gives the period of oscillation one would measure upon taking a strip with $L \gg R$ and pinning its ends at distance λ in the laboratory. A three-dimensional visualization of such a strip appears in Figure 3(b).

We conclude that long strips with metric gradients minimize their energy by curling up like telephone cords. They deviate from this quasi-uniform solution only when they must maneuver near the ends to obey boundary conditions, or form a kink in the middle to produce a solution with no net twist.

Returning to the general case where $C_1 \neq C_2$ and writing out the Euler–Lagrange equations, we find that the uniform configuration (26) is still a solution. The energy density is given by $\mathcal{E} = C_2 \tan^2 \theta / 2R^2$ and all other features of the global minimum such as the period of oscillation remain unchanged.

III. GEOMETRICAL CONSIDERATIONS

The strip problem was originally motivated by experiments on two-dimensional sheets of deformed material. The expectation was that by focusing upon a long thin strip, one could understand basic geometrical features of the full two-dimensional problem. Now that we have obtained a reasonably detailed account of the ground state of the strip, it is clear that its significance for the original problem is limited. Long thin strips wrap up in a helix, like a telephone cord. This geometry is impossible for the edges of a flower or a leaf. Therefore, in Section IV we return to the two-dimensional problem and search for some alternate approaches. As preparation, this section summarizes some basic facts concerning the differential geometry of surfaces.

Let $\vec{r} = (x, y, z)$ be a point in three-dimensional Euclidean space, where x , y , and z are the usual Cartesian coordinates with respect to a fixed laboratory frame. A surface may then be defined in parametric form by

$$\vec{r} = \vec{r}(u, v) = (x(u, v), y(u, v), z(u, v)) \quad (31)$$

where u and v are parameters whose range is not specified for the moment. Throughout this section, derivatives will be abbreviated by $\partial_1 = \partial/\partial u$ and $\partial_2 = \partial/\partial v$. The elements of the metric tensor are then defined from

$$g_{\alpha\beta} = (\partial_\alpha \vec{r}) \cdot (\partial_\beta \vec{r}). \quad (32)$$

A second fundamental form (tensor) is defined as follows: Let $\hat{r}_3 = \hat{r}_3(u, v)$ be the unit vector that is perpendicular to the surface at point (u, v) and varies continuously with u and v . The elements of the second fundamental form are then given by

$$d_{\alpha\beta} = \hat{r}_3 \cdot \partial_\alpha \partial_\beta \vec{r}. \quad (33)$$

The two symmetric tensors $g_{\alpha\beta}$ and $d_{\alpha\beta}$ play a significant role in the theory of surfaces, as is apparent in standard texts[7, 11].

A. Trumpets

In order to gain familiarity with the types of surfaces studied in Section IV, we first consider an elementary example defined by

$$\vec{r} = \rho(v)(\cos u \hat{e}_1 + \sin u \hat{e}_2) + \zeta(v) \hat{e}_3, \quad (34)$$

where \hat{e}_1 , \hat{e}_2 , and \hat{e}_3 are constant unit vectors along the three axes of the laboratory frame, while $\rho(v)$ and $\zeta(v)$ are functions of v alone, and are further restricted by the condition

$$\rho'^2 + \zeta'^2 = 1, \quad (35)$$

where the primes indicate derivatives with respect to v . The surface is thus specified by the single function $\rho = \rho(v)$. In particular, the metric tensor is then given by

$$g_{11} = \rho^2, \quad g_{22} = 1, \quad g_{12} = 0. \quad (36)$$

In order to calculate the second fundamental form, we first construct the orthonormal trihedral

$$\begin{aligned} \hat{r}_1 &= \frac{1}{\rho} \partial_1 \vec{r} = -\sin u \hat{e}_1 + \cos u \hat{e}_2 \\ \hat{r}_2 &= \partial_2 \vec{r} = \rho'(\cos u \hat{e}_1 + \sin u \hat{e}_2) + \sqrt{1 - \rho'^2} \hat{e}_3 \\ \hat{r}_3 &= \sqrt{1 - \rho'^2}(\cos u \hat{e}_1 + \sin u \hat{e}_2) - \rho' \hat{e}_3, \end{aligned} \quad (37)$$

where \hat{r}_1 and \hat{r}_2 are tangent to the surface, while $\hat{r}_3 = \hat{r}_1 \times \hat{r}_2$ is perpendicular. The second fundamental form is then calculated from Eq. (33) to yield

$$\begin{aligned} d_{11} &= -\rho \sqrt{1 - \rho'^2}, \quad d_{22} = \frac{\rho''}{\sqrt{1 - \rho'^2}} \\ d_{12} &= d_{21} = 0 \end{aligned} \quad (38)$$

A special case of this class of surfaces is the ordinary cylinder with unit radius, obtained with the choice $\rho = 1$ and $\zeta = v$. The metric is then Euclidean ($g_{11} = 1 = g_{22}$, $g_{12} = g_{21} = 0$) and the elements of the second fundamental form are $d_{11} = -1$, $d_{22} = 0$, $d_{12} = d_{21} = 0$.



FIG. 4: Rendering of the surface produced by the metric in Eq. (39) for $u \in [0, 2\pi]$, and $v \in (-\infty, 0]$ (in color).

A more interesting example is obtained by the choice

$$\sqrt{g_{11}} = \rho = 1 + \frac{1}{1-v}, \quad (39)$$

which leads to an axially symmetric surface with variable radius $\rho = \rho(v)$ and height $z = \zeta(v)$ calculated from Eq. (35). This surface reduces to the ordinary cylinder in the limit $v \rightarrow -\infty$, but its radius increases with increasing v (or z). It would appear that the radius of this surface would eventually grow to infinity as $v \rightarrow 1$. Actually, this limit cannot be obtained because of a singularity that develops earlier when $\rho'^2 = 1$ or $v = 0$. The actual surface is illustrated in Figure 4; we will refer to it as the *trumpet*. It starts as a cylinder with radius $\rho = 1$ and terminates at a cusp with radius $\rho = 2$. Near the cusp the elements of the second fundamental form calculated from Eq. (38) approach the characteristic limits $d_{11} \rightarrow 0$, $d_{22} \rightarrow \infty$, while d_{12} vanishes everywhere.

This trumpet may be considered the most primitive model of a flower. However, a true flower is a trumpet that is allowed to grow beyond the cusp, and displays numerous ripples, because biology and elasticity dictate slight modifications of the metric and second fundamental form needed to evade the singularity. Geometry alone cannot resolve what happens as one tries to push a surface beyond such a cusp, but may help to classify the possibilities.

Hence, in the remainder of this section, we formulate an inverse problem of sorts that will enable us to interpret the explicit results of Section IV.

B. Compatibility conditions

The elementary example we have just considered is significantly generalized by considering surfaces for which the coordinate curves form an *orthogonal net*, which means that they are characterized by a metric of the form

$$g_{11} = g_{11}(u, v), \quad g_{22} = g_{22}(u, v), \quad g_{12} = 0. \quad (40)$$

The corresponding orthonormal trihedral is then defined from

$$\hat{r}_1 = \frac{\partial_1 \vec{r}}{\sqrt{g_{11}}}, \quad \hat{r}_2 = \frac{\partial_2 \vec{r}}{\sqrt{g_{22}}}, \quad \hat{r}_3 = \hat{r}_1 \times \hat{r}_2. \quad (41)$$

We now consider the elementary integrability condition

$$\begin{aligned} \partial_1 \partial_2 \vec{r} &= \partial_2 \partial_1 \vec{r} \\ \Rightarrow \partial_1(\sqrt{g_{22}} \hat{r}_2) &= \partial_2(\sqrt{g_{11}} \hat{r}_1) \\ \Rightarrow (\partial_1 \sqrt{g_{22}}) \hat{r}_2 + \sqrt{g_{22}} \partial_1 \hat{r}_2 &= (\partial_2 \sqrt{g_{11}}) \hat{r}_1 + \sqrt{g_{11}} \partial_2 \hat{r}_1 \end{aligned} \quad (42)$$

Contracting both sides of Eq. (42) with the unit vectors \hat{r}_1 , \hat{r}_2 and \hat{r}_3 in turn we obtain

$$(\hat{r}_1 \cdot \partial_1 \hat{r}_2) = \frac{\partial_2 \sqrt{g_{11}}}{\sqrt{g_{22}}} \quad (43a)$$

$$(\hat{r}_2 \cdot \partial_2 \hat{r}_1) = \frac{\partial_1 \sqrt{g_{22}}}{\sqrt{g_{11}}} \quad (43b)$$

$$\sqrt{g_{11}}(\hat{r}_3 \cdot \partial_2 \hat{r}_1) = \sqrt{g_{22}}(\hat{r}_3 \cdot \partial_1 \hat{r}_2). \quad (43c)$$

We observe that for $\sqrt{g_{11}} = 1 - v/R$, $g_{22} = 1$, Eq. (43a) reproduces Eq. (5). As in Section II, we parameterize the trihedral with the Euler angles of Eq. (7) to obtain the three fundamental equations

$$\cos \theta \partial_1 \phi + \partial_1 \psi = -\frac{\partial_2 \sqrt{g_{11}}}{\sqrt{g_{22}}} \quad (44a)$$

$$\cos \theta \partial_2 \phi + \partial_2 \psi = \frac{\partial_1 \sqrt{g_{22}}}{\sqrt{g_{11}}} \quad (44b)$$

$$\begin{aligned} \sqrt{g_{11}}(-\sin \theta \cos \psi \partial_2 \phi + \sin \psi \partial_2 \theta) \\ = \sqrt{g_{22}}(\sin \theta \sin \psi \partial_1 \phi + \cos \psi \partial_1 \theta), \end{aligned} \quad (44c)$$

which will provide the basis for subsequent development. It should be noted that the compatibility conditions Eqs. (44) are formulated entirely in terms of the metric tensor $g_{\alpha\beta}$ and that the elements of the second fundamental form do not appear explicitly. In fact, once a solution of Eqs. (44) is available, $d_{\alpha\beta}$ can be computed from Eq. (33) as

$$\begin{aligned} d_{11} &= \sqrt{g_{11}}(\hat{r}_3 \cdot \partial_1 \hat{r}_1) \\ &= \sqrt{g_{11}}(-\sin \theta \cos \psi \partial_1 \phi + \sin \psi \partial_1 \theta) \end{aligned} \quad (45a)$$

$$\begin{aligned} d_{22} &= \sqrt{g_{22}}(\hat{r}_3 \cdot \partial_2 \hat{r}_2) \\ &= \sqrt{g_{22}}(\sin \theta \sin \psi \partial_2 \phi + \cos \psi \partial_2 \theta) \end{aligned} \quad (45b)$$

$$\begin{aligned} d_{12} &= \sqrt{g_{22}}(\hat{r}_3 \cdot \partial_1 \hat{r}_2) \\ &= \sqrt{g_{22}}(\sin \theta \sin \psi \partial_1 \phi + \cos \psi \partial_1 \theta) \end{aligned} \quad (45c)$$

$$\begin{aligned} d_{21} &= \sqrt{g_{11}}(\hat{r}_3 \cdot \partial_2 \hat{r}_1) \\ &= \sqrt{g_{11}}(-\sin \theta \cos \psi \partial_2 \phi + \sin \psi \partial_2 \theta) \end{aligned} \quad (45d)$$

Note that the symmetry condition $d_{12} = d_{21}$ is not explicit in Eq. (45), but is enforced by Eq. (44c).

As an elementary illustration, we return to the case of a trumpet characterized by a metric of the form $\sqrt{g_{11}} = \rho(v)$, $\sqrt{g_{22}} = 1$, and $g_{12} = 0$. It is straightforward to verify that

$$\psi = 0, \phi = \pi/2 + u, \cos \theta = -\rho', \sin \theta = \sqrt{1 - \rho'^2} \quad (46)$$

is a solution of Eqs. (44) that reproduces the trumpet discussed earlier in this section.

Our aim in Section III C is to show that Eqs. (44) can be used as evolution equations actually to calculate trumpet-like solutions for the general class of metrics given by Eq. (40) through the solution of an initial value problem. The connection with the standard Gauss–Codazzi compatibility conditions[7] is briefly discussed in Section III D.

C. Evolution equations

Consider the trumpet with metric given by Eq. (39). When $v \rightarrow -\infty$, the surface approaches a cylinder. Can one choose some large negative value of v , suppose that the surface for this value of v is a circle, and integrate towards $v = 0$ knowing nothing but the metric and reconstruct the trumpet? The answer is yes. One can find three first-order equations that express the changes of θ , ψ , and ϕ with respect to v and integrate them forward as if v is a time variable.

Finding the equations is not completely straightforward. Eqs. (44) consist in three first-order partial differential equations for the three Euler angles θ , ψ , and ϕ . However since Eq. (44a) involves derivatives in u only, algebraic manipulation alone does not allow one to solve for $\partial_2 \theta$, $\partial_2 \psi$, and $\partial_2 \phi$.

Note that derivatives of ϕ appear in Eqs. (44) but not ϕ itself. One can use the first two of Eqs. (44) to express $\partial_1 \phi$ and $\partial_2 \phi$ in terms of the other two Euler angles. Removing ϕ in this way is only permitted, however, if after solving for $\partial_1 \phi$ and $\partial_2 \phi$ one imposes the condition $\partial_1 \partial_2 \phi = \partial_2 \partial_1 \phi$ to obtain

$$\begin{aligned} & (\sqrt{g_{11} g_{22}} \partial_1 \psi + \sqrt{g_{11}} \partial_2 \sqrt{g_{11}}) \partial_2 \theta - \sqrt{g_{22}} G \cot \theta \\ &= (\sqrt{g_{11} g_{22}} \partial_2 \psi - \sqrt{g_{22}} \partial_1 \sqrt{g_{22}}) \partial_1 \theta, \end{aligned} \quad (47)$$

where

$$\begin{aligned} G &= \frac{\sqrt{g_{11}}}{g_{22}} (\partial_2 \sqrt{g_{11}}) \partial_2 \sqrt{g_{22}} + \frac{1}{\sqrt{g_{11}}} (\partial_1 \sqrt{g_{11}}) \partial_1 \sqrt{g_{22}} \\ &- \partial_1 \partial_1 \sqrt{g_{22}} - \frac{\sqrt{g_{11}}}{\sqrt{g_{22}}} \partial_2 \partial_2 \sqrt{g_{11}} \end{aligned} \quad (48)$$

One now solves the three Eqs. (44) and Eq. (47) for $\partial_2 \theta$, $\partial_2 \psi$, $\partial_1 \phi$ and $\partial_2 \phi$. In expressing the results, it is convenient to use the expressions for the second fundamental form in Eq. (45) as shorthand for combinations of derivatives. One obtains

$$\partial_2 \theta = \frac{d_{12} \partial_1 \theta + G \cos \psi}{d_{11}} \quad (49a)$$

$$\begin{aligned} \partial_2 \psi &= \frac{1}{d_{11}} \left[\frac{\partial_1 \sqrt{g_{22}}}{\sqrt{g_{11}}} d_{11} - \cos \theta d_{12} \partial_1 \phi \right. \\ &\quad \left. - G \sin \psi \cot \theta \right] \end{aligned} \quad (49b)$$

$$\partial_2 \phi = \frac{\partial_1 \sqrt{g_{22}}}{\cos \theta \sqrt{g_{11}}} - \frac{\partial_2 \psi}{\cos \theta}. \quad (49c)$$

These are the basic evolution equations for the Euler angles. Whenever $\partial_1 \phi$ appears, it should be viewed as shorthand for

$$\partial_1 \phi = -\frac{\sqrt{g_{22}} \partial_1 \psi + \partial_2 \sqrt{g_{11}}}{\sqrt{g_{22}} \cos \theta}. \quad (49d)$$

The procedure for constructing surfaces progresses as follows: We specify the values of θ , ψ , and ϕ for all u and some value of $v = v_0$. To construct a trumpet, we choose v_0 sufficiently negative so that we can use the expressions for cylinder $\psi = 0$, $\phi = \pi/2 + u$, and $\theta = \pi/2$ to set initial values of the Euler angles for $u \in [0, 2\pi]$. Next, we calculate the right hand sides of Eqs. (49) using these initial values, and update each Euler angle through explicit Euler integration, $\theta(v + dv) = \theta(v) + \partial_2 \theta dv$. It is easy to construct the surface \vec{r} . To do so, form the trihedral from the Euler angles through Eq. (7). Then from Eq. (41) one has

$$\partial_2 \vec{r} = \sqrt{g_{22}} \hat{r}_2, \quad (50)$$

which means that if the surface is specified on the line $v = v_0$, its future evolution can be determined as well.

The integration process is extremely rapid. We have used it in order to reproduce the trumpet depicted in Figure 4. The process of integrating forward terminates at $v = 0$ because d_{11} vanishes there for all u , and two denominators in Eq. (49) become singular.

We have also used the equations to generate surfaces from more general metrics, and a characteristic result is exhibited in Figure 5. Here we chose the metric

$$\sqrt{g_{11}} = 1 + \frac{1}{1-v} (1 + \frac{1}{2} \cos 3u); \quad g_{22} = 1. \quad (51)$$

The surface has a slight three-fold modulation that is quite clear if one plots Euler angles, but rather faint when one looks at the surface itself. As in the case of the trumpet, the integration process stops near to $v = 0$. Examining the reason, one finds that once again d_{11} vanishes. This three-fold trumpet does not have cylindrical symmetry, and d_{11} does not vanish simultaneously for all u . Instead, it first vanishes for three values of u . However, the evolution equations are singular and cannot be integrated past this point. Our original hope had been to use evolution equations to obtain flower-like solutions such as the one displayed in Figure 8. Unfortunately, the rippling edge necessarily involves an oscillation in curvature, and d_{11} must oscillate in sign where ripples are visible. Thus our integration procedure is intrinsically unable to obtain solutions of this type. However, through trials with the evolution equations, we have found that they successfully create surfaces over ranges of u and v where d_{11} does not vanish.

We note in closing that it is not difficult to generalize the equations of this section to the case where $g_{12} \neq 0$. One takes

$$\hat{r}_2 = \frac{\partial_2 \vec{r} / \sqrt{g_{22}} - (\hat{r}_1 / \sqrt{g_{22}}) \partial_2 \vec{r} \cdot \hat{r}_1}{\sqrt{1 - g_{12}^2 / g_{11} g_{22}}} \quad (52)$$

and otherwise proceeds as before. The resulting expressions are somewhat lengthy, and as we have not made use of them, we do not record them here.



FIG. 5: Three-fold trumpet produced by integrating Eqs. (49) forward from a cylindrically symmetric initial condition at $v_0 = -2\pi$, using the metric in Eq. (51) (in color).

D. Gauss-Codazzi

Our treatment has been based upon the compatibility conditions Eq. (42) which are formulated purely in terms of the metric tensor $g_{\alpha\beta}$, while the second fundamental tensor is a derived quantity displayed in Eq. (45). By contrast, both tensors $g_{\alpha\beta}$ and $d_{\alpha\beta}$ appear as fundamental variables in the formulation of the Gauss–Codazzi compatibility conditions employed in standard treatments[7]. It would then be interesting to demonstrate that the Gauss–Codazzi equations can actually be derived starting from the compatibility conditions Eq. (42) and the definitions Eq. (45).

As an example, we write the first two conditions in Eq. (42) as

$$\begin{aligned}\partial_1\psi &= -\cos\theta\partial_1\phi - \frac{\partial_2\sqrt{g_{11}}}{\sqrt{g_{22}}} \\ \partial_2\psi &= -\cos\theta\partial_2\phi + \frac{\partial_1\sqrt{g_{22}}}{\sqrt{g_{11}}}\end{aligned}\quad (53)$$

and impose the integrability condition $\partial_1\partial_2\psi = \partial_2\partial_1\psi$ to obtain

$$\begin{aligned}\sin\theta(\partial_1\theta\partial_2\phi - \partial_1\phi\partial_2\theta) \\ = -\left[\partial_1\left(\frac{\partial_1\sqrt{g_{22}}}{\sqrt{g_{11}}}\right) + \partial_2\left(\frac{\partial_2\sqrt{g_{11}}}{\sqrt{g_{22}}}\right)\right].\end{aligned}\quad (54)$$

On the other hand, a straightforward application of definitions (45) together with Eq. (54) yields

$$\begin{aligned}d_{11}d_{22} - d_{12}d_{21} &= R_{1212}, \\ R_{1212} &= -\sqrt{g_{11}g_{22}}\left[\partial_1\left(\frac{\partial_1\sqrt{g_{22}}}{\sqrt{g_{11}}}\right) + \partial_2\left(\frac{\partial_2\sqrt{g_{11}}}{\sqrt{g_{22}}}\right)\right],\end{aligned}\quad (55)$$

where R_{1212} is indeed the correct expression for the Riemann tensor element associated with a metric in the form of Eq. (40). Thus Eq. (56) reproduces the celebrated Gauss equation.

We have not yet attempted a corresponding derivation of the two Codazzi equations starting from our Eqs. (42) and (45) but merely state here all three Gauss–Codazzi equations in

symbolic form:

$$\begin{aligned}d_{22} &= \frac{d_{12}^2 + R_{1212}}{d_{11}} \\ \partial_2d_{11} &= \partial_1d_{12} + d_{1\gamma}\left\{\begin{matrix}\gamma \\ 12\end{matrix}\right\} - d_{2\gamma}\left\{\begin{matrix}\gamma \\ 11\end{matrix}\right\} \\ \partial_2d_{12} &= \partial_1d_{22} - d_{2\gamma}\left\{\begin{matrix}\gamma \\ 12\end{matrix}\right\} + d_{1\gamma}\left\{\begin{matrix}\gamma \\ 22\end{matrix}\right\},\end{aligned}\quad (56)$$

where $\left\{\begin{matrix}\gamma \\ \alpha\beta\end{matrix}\right\}$ are the Christoffel symbols. Eqs. (56) are again written in the form of evolution equations and can be solved with initial conditions starting at $v \rightarrow -\infty$ given the ordinary cylinder values $d_{11} = -1$, $d_{22} = 0$ and $d_{12} = 0$. Once a solution of Eqs. (56) is obtained at some finite v , the actual construction of the surface proceeds through the solution of a compatible system of linear equations: see Eqs. (39.8) of Ref. [7].

IV. GROUND STATE FOR FLOWERS

A. Numerical technique

We now return to techniques employed recently[5] for the construction of surfaces through minimization of an elastic energy functional, and examine again the results in light of what we learned in Section III. We begin by defining more carefully than has been done previously the problem that needs to be solved. In rough outline, one wants to take a thin flat sheet of material, impose a new metric $g_{\alpha\beta}$ upon it, and ask how it deforms in response. A more precise specification of the problem follows:

Differential geometry describes a mapping between two spaces: a reference configuration described by variables (u, v) , and a surface described by $\vec{r}(u, v)$. Experiments on deformed surfaces are performed by taking a flat sheet of material, deforming it in some controlled way, and then allowing the material to buckle in space. To construct a numerical model of the system we will first describe the reference state, corresponding to undeformed material, and then a discrete set of variables that describes a sheet of material moving about in three dimensions.

The experimental reference state consists in a flat slab of material, much wider and longer than it is thick. Imagine therefore positions in a thin sheet described by (x, y, z) , where $z \in [0, t]$, and the thickness t is small. Pick N points within this sheet, and label them by $\vec{r}_i^0 = (x_i, y_i, z_i)$, where i ranges from 1 to N . In practice, we will take these points to sit on regular lattices, but they could be randomly distributed. Each point \vec{r}_i^0 has a number of near neighbors: label these near neighbors with $j \in n(i)$. Describe the vector between two near neighbors by $\vec{r}_{ij}^0 = \vec{r}_j^0 - \vec{r}_i^0$. We can now write down an energy functional which is constructed precisely so that its ground state gives back this reference configuration. This functional is defined on a new collection of variables \vec{r}_i , where again i ranges from 1 to N , and the neighbor list $j \in n(i)$ is the same as in the reference configuration. Now, however, the points \vec{r}_i are free to move anywhere in three-dimensional

space. One can think of them as describing arbitrary deformations of the original thin sheet. If a particle i has particle j as a neighbor in the reference configuration, then particle j remains in the list of neighbors no matter how the sheet deforms.

The significance of neighbors is provided by an energy functional that depends upon the squared distance between pairs of neighbors. Define $\vec{r}_{ij} = \vec{r}_j - \vec{r}_i$; then

$$U_0 = \frac{1}{4} \sum_{ij} (|\vec{r}_{ij}|^2 - |\vec{r}_{ij}^0|^2)^2. \quad (57)$$

By construction this energy functional has the property that if every particle \vec{r}_i returns to the reference location \vec{r}_i^0 , then the energy is zero. This ground state is not unique, for the energy is also unchanged if the locations of all the particles are rotated and translated in three-dimensional space, as when one picks up a piece of cardboard and translates and rotates it. Depending upon details involving the numbers of neighbors of each particle, there may be additional degeneracies in the ground state as well, but we will not worry about this point right now.

Our numerical model for deforming the sheet is to go to each bond and stretch it so that the square distance between near neighbors i and j adopts the new value l_{ij}^2 . Thus we have the energy functional

$$U = \frac{1}{4} \sum_{ij} (|\vec{r}_{ij}|^2 - l_{ij}^2)^2, \quad (58)$$

and direct minimization of U has been employed to obtain most of the three-dimensional figures in this paper.

In order to connect Eq. (58) with the discussion in the previous sections, we must explain the connection between bond lengths l_{ij} and metrics. We use the following prescription. For each bond ij , choose values of u and v through

$$u_{ij} = \hat{e}_1 \cdot (\vec{r}_i^0 + \vec{r}_j^0)/2; v_{ij} = \hat{e}_2 \cdot (\vec{r}_i^0 + \vec{r}_j^0)/2. \quad (59)$$

In other words, take u and v to be the x and y coordinates of the midpoints of bonds in the reference configuration. We define a *target metric* through three functions

$$g_{11}^t(u, v), g_{22}^t(u, v), \text{ and } g_{12}^t(u, v). \quad (60)$$

One could choose, for example the functions in Eq. (36) if one wanted to recover a trumpet. Using the target metric, one obtains a new equilibrium length squared l_{ij}^2 for the bond between points i and j through

$$l_{ij}^2 = \sum_{\alpha\beta} \vec{r}_{ij}^{0\alpha} g_{\alpha\beta}^t(u_{ij}, v_{ij}) \vec{r}_{ij}^{0\beta}. \quad (61)$$

So, for example, if a bond in the reference configuration lies along the x axis at position (u, v) given by Eq. (59), its new length is $\sqrt{g_{11}^t(u, v)}$. The reason that we call $g_{\alpha\beta}^t$ the target metric rather than the metric is that one can put any collection of particle locations one wishes into the functional Eq. (58), not just particle locations that correspond to surfaces with metric $g_{\alpha\beta}^t$. Thus the metric of the surface obtained through

numerical minimization may in principle be different from the target. We will be attempting to determine whether the ground states of U produce surfaces whose metric equals the target metric.

One might wonder why U involves squares of bond lengths, rather than $(r_{ij} - l_{ij})^2$. The answer is that Eq. (58) leads to conventional nonlinear elasticity in the continuum limit, while the alternative does not. To obtain the continuum limit, let $\vec{r}(u, v)$ be a continuous vector field, and write

$$\vec{r}_{ij} \approx (\vec{r}_{ij}^0 \cdot \vec{\nabla}) \vec{r}. \quad (62)$$

Recalling Eq. (32), substitute Eq. (62) into Eq. (58) to obtain

$$U = \frac{1}{4} \sum_{ij} \left[\sum_{\alpha\beta} \vec{r}_{ij}^{0\alpha} (g_{\alpha\beta} - g_{\alpha\beta}^t) \vec{r}_{ij}^{0\beta} \right]^2; \quad (63)$$

that is, the energy is given by subtracting the target metric from the actual metric, and vanishes when the two are equal. From Eq. (63) one sees that the appropriate generalization of the Lagrangean strain tensor to situations with target metrics is

$$E_{\alpha\beta} = \frac{1}{2} (g_{\alpha\beta} - g_{\alpha\beta}^t). \quad (64)$$

If the target metric is a unit tensor, E reduces to the conventional Lagrangean strain tensor of nonlinear elasticity, and when deformations are small it reduces further to the strain tensor of linear elasticity. One can write

$$U = \sum_{ij} \left[\sum_{\alpha\beta} \vec{r}_{ij}^{0\alpha} E_{\alpha\beta} \vec{r}_{ij}^{0\beta} \right]^2. \quad (65)$$

For a particular arrangement of mass points, one can perform the sums over \vec{r}^0 and obtain a specific quadratic functional depending upon the components of E [5]. We do not need these expressions here and will not pursue them further.

However, we will spell out the particular reference configuration \vec{r}_i^0 that has been used to produce results for this paper. It consists in either one or two layers of a triangular lattice. To be completely explicit, use three integers lmn to describe the point locations rather than the single index i :

$$\vec{r}_{lmn}^0 = (1, 0, 0)l + (\frac{1}{2}, \frac{\sqrt{3}}{2}, 0)m + (\frac{1}{\sqrt{3}}, 0, \sqrt{\frac{2}{3}})n, \quad (66)$$

where l and m range over positive and negative integers, and n equals 0 to produce a single layered structure, or ranges over 0 and 1 to produce a two-layered structure. In the two-layered structure, each particle has nine nearest neighbors, each at unit distance; six with the same value of n on the same horizontal sheet, and three with a different value of n on a different horizontal sheet. In these crystalline structures, the near neighbors of particle i are all the particles j for which $|\vec{r}_{ij}^0|^2 = 1$.

We record one final technical point about the numerical techniques. Given particle locations \vec{r}_i , we will want to view the particles as describing a continuous surface, and to construct its metric. To do so, focus on the lower sheet of particles

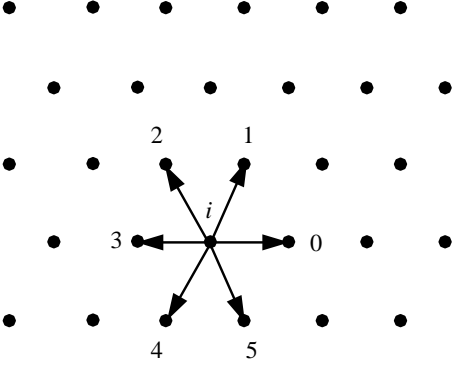


FIG. 6: Enumeration of neighbors surrounding point i , used to describe the construction of numerical metrics in Eq. (68). The diagram shows the particles sitting in the reference configuration \tilde{r}_i^0 described by Eq. (66).

($n = 0$ in Eq. (66)) and label the neighbors of particle i as in Figure 6. Denote by δr_0^2 the square distance from point i to the neighbor located at 0 in the figure and so on for the remaining five neighbors. Then we have numerical representations of the metric

$$\begin{aligned} g_{11} &= \frac{\delta r_0^2 + \delta r_3^2}{2} \\ g_{22} &= \frac{\delta r_1^2 + \delta r_2^2 + \delta r_4^2 + \delta r_5^2 - \delta r_0^2/2 - \delta r_3^2/2}{3} \\ g_{12} &= \frac{\delta r_1^2 - \delta r_2^2 - \delta r_4^2 + \delta r_5^2}{2\sqrt{3}} \end{aligned} \quad (67)$$

B. Numerical experiments

The questions we wish to pose about target metrics are:

1. What are the ground states of Eq. (63)?
2. When do these ground states correspond to smooth surfaces in the continuum limit?
3. When the ground state is a smooth surface, under what conditions does the target metric equal the metric of the surface?

Observe that ground states of Eq. (63) always exist. The functional is positive definite, and for a finite number of particles must have one or more global minima. If the reference configuration does not have bending stiffness, however, the resulting ground state corresponds to a nondifferentiable surface. To illustrate this point, we use Eq. (39) as a target metric, and work on the domain

$$u \in [0, 2\pi], \quad \text{and} \quad v \in [-3\pi, 0]. \quad (68)$$

We represent the system with a reference crystal 200 columns long, 346 rows high, but only 1 layer thick (in Eq. (66),



FIG. 7: Image of surface created by minimizing Eq. (63) for a reference crystal with $200 \times 346 \times 1$ particles, and target metric given by Eq. (69). The surface achieves the target; the total energy summed over all particles is less than 10^{-2} . However, the solution is nowhere smooth, and resembles tree bark. It can be understood as an embedding of the target metric whose first derivative is nowhere continuous (in color).

$l \in [0, 200], m \in [0, 346], n = 0$). Since the reference configuration is infinitely thin, there is no source of bending stiffness. Using the target metric

$$\begin{aligned} g_{11}^t(u, v) &= 1 + \frac{1}{1-v} \\ g_{22}^t(u, v) &= 1 \\ g_{12}^t(u, v) &= 0 \end{aligned} \quad (69)$$

we minimize U , and the result is displayed in Figure 7. The total energy U has converged below 10^{-2} , and each bond has reached its target value to better than two parts in 10^4 . However, the surface is not smooth, nor is the configuration displayed in the figure plausibly unique. As we know from Section III A, there do exist smooth surfaces whose metric equals this target metric, but the minimization routine under these conditions does not find them. Venkataramani *et al.*[12] have pointed out the existence of non-smooth surfaces of the sort appearing in the figure.

Low energy states of Eq. (63) look very different when one moves from reference crystals with one layer to reference crystals with two layers (In Eq. (66), $n \in [0, 1]$). Now the system possesses some stiffness, and pays an energy penalty for bending too rapidly. Once again minimizing Eq. (63) for the parameter range in Eq. (68), we find the minimum energy state that is essentially the trumpet shown in Figure 4. The energy of this structure is 74.3; it cannot converge to zero, since springy elastic material has been wrapped into a cylinder.

We compared the metric g as computed through Eq. (68) with the target metric g^t for the structure in Figure 4. For each metric component, the difference is featureless, and approximately equal to -3×10^{-2} at every point, due to a slight compression needed to bend the inner layer of the reference crystal into a cylinder. We conclude from the numerical calculations that the metric and target metric are equal within numerical accuracy. We emphasize that in Section III C we reproduced the trumpet in Fig. 4 through evolution equations; the metric and boundary conditions suffice to determine the surface in this case.

As a more interesting exercise in direct minimization of Eq. (63), we extend the domain beyond the critical point and



FIG. 8: Image of surface created by minimizing Eq. (63) for a reference crystal with $200 \times 346 \times 2$ particles, and target metric given by Eq. (69), corresponding to a domain where v varies from -3π to $\frac{1}{2}$. Once $v > 0$, trumpet solutions given by Eq. (34) no longer exist, and the evolution equations in Eq. (49) are incapable of finding solutions. The minimum energy state is the smooth flower-like surface with seven-fold symmetry displayed here. As shown in Figure 9, the metric of this surface does not equal the target metric. Creation of this surface required long series of minimizations. The process began by placing particles in a cylinder with a Euclidean metric, and very slowly changing the metric until it reached the desired target value, continually minimizing the functional Eq. (63) along the way. Attempts to find the surface more quickly resulted in higher-energy structures with creases (in color).

look for a solution in

$$u \in [0, 2\pi], \quad \text{and} \quad v \in [-3\pi, \frac{1}{2}]. \quad (70)$$

The significance of increasing the range of v is that the theory of Section III A is unable to find a smooth surface for $v > 0$. In contrast, upon minimizing U once more, we find the flower-like surface shown in Figure 8. Now when we subtract the target metric Eq. (69) from the metric actually achieved, Eq. (68), the difference is visible, as shown in Figure 9. The seven-fold pattern in the surface is reflected in seven-fold oscillations in g_{11} and g_{22} . The off-diagonal component of the tensor, g_{12} , remains zero within numerical accuracy. We conclude that in this case, no smooth surface is able to reproduce the target metric, and numerical minimization finds a metric close to the target that is capable of producing a smooth surface even for $v > 0$. We see no reason that this surface should be considered unique. In all likelihood, its details depend upon the thickness of the sheet. According to Audoly and Boudaoud[4], one should expect the surface to be increasingly ramified as its thickness diminishes.

As a final exercise, we took the metric components computed numerically and depicted in Fig. 9, inserted them into the evolution equations Eqs. (49) and attempted to reproduce the structure in Figure 8. This attempt was only partially successful. The evolution equations were unable to proceed past points where d_{11} approached zero. It is clearly possible for d_{11} to vanish without a surface developing singular cusps at that point, but our numerical routines would require very del-

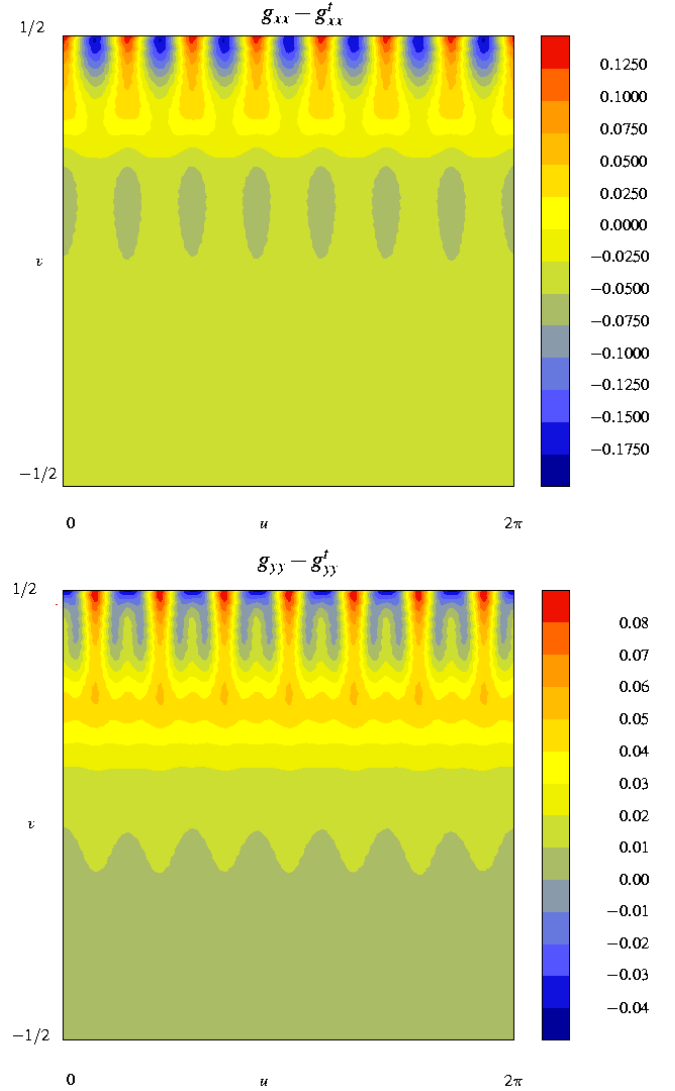


FIG. 9: Metric component deviations for the flower depicted in Figure 8. Each panel shows a contour plot of the difference between the metric component $g_{\alpha\beta}$ and the target metric $g_{\alpha\beta}^t$. The off-diagonal metric element g_{12} is not illustrated because its numerical values are too small to be discerned at the scale of the figure (in color).

icate cancellations in order to proceed past such a point.

V. CONCLUSIONS

Given a surface, it is completely straightforward to compute the metric. The inverse problem of finding surfaces compatible with a given metric is much more difficult. In setting out on the studies recorded in this paper, we had two goals. First, we wanted finally to determine the low-energy configurations of long strips with linear gradients in metric. This we have accomplished. Second, we hoped to determine conditions on the relatively simple metrics thought to create the shapes of leaves and flowers[1] that would enable surfaces to be reconstructed.

In the second task we have been only partially successful. We found evolution equations enabling construction of surfaces from initial conditions and metric alone. However, at points when d_{11} , a component of the second fundamental form, vanishes, the equations become singular and cannot be integrated further. We are unable to tell when this singularity really reflects the impossibility of creating a surface compatible with the metric, and when it simply reflects a technical defect in the method of construction.

Some intuitive understanding of this situation can be obtained by thinking about a piece of paper, with flat Euclidean metric. Imagine holding the bottom of the paper completely straight, along the u axis, while the left edge of the paper runs along the v axis. There is an infinite number of shapes the paper can take, which correspond to all different bends possible at different points along v around axes parallel to u . All of these solutions have vanishing curvature in the u direction; $d_{11} = 0$, and the evolution equations (49) accordingly are unable to make any predictions. That is, in some cases the vanishing of d_{11} can correspond to a genuine uncertainty, based upon initial conditions, concerning how the surface should

evolve.

On the other hand, for the surface in Figure 8, the curvature d_{11} oscillates in sign and therefore passes through zero, yet the surface exists. Therefore, the vanishing of d_{11} can be compatible with the existence of a surface even if our purely geometrical methods cannot find it beyond points where $d_{11} = 0$. Minimization of Eq. (58) still produces a surface because elasticity resolves the questions that cannot be answered by geometry.

Acknowledgments

Most of this work was carried out within the stimulating environment of the Roussos Center for Nonlinear Dynamics, and was influenced in part by the Hydrangeas at Boukari, Corfu. M.M. is grateful for financial support from the National Science Foundation, DMR-0401766, and the Research Center of Crete.

-
1. E. Sharon, B. Roman, M. Marder, G.-S. Shin, and H. L. Swinney, *Nature* **419**, 579 (2002).
 2. M. Marder, *The shape of the edge of a leaf*, cond-mat/0208232 (2002).
 3. B. Audoly and A. Boudaoud, *Comptes Rendus Mecanique* **330**, 1 (2002).
 4. B. Audoly and A. Boudaoud, *Physical Review Letters* **91**, 086105/1 (2003).
 5. M. Marder, *Foundations of Physics* **33**, 1743 (2003).
 6. M. Marder, E. Sharon, S. Smith, and B. Roman, *Europhysics Letters* **62**, 498 (2003).
 7. E. P. Eisenhart, *An introduction to differential geometry, with use of the tensor calculus* (Princeton University Press, Princeton, 1959).
 8. E. Sharon, M. Marder, and H. L. Swinney, *American Scientist* **92**, 254 (2004).
 9. H. Goldstein, *Classical Mechanics* (Addison-Wesley, Reading, MA, 1969).
 10. J. Chovan, N. Papanicolaou, and S. Komineas, *Physical Review B* **65**, 064433 (2002).
 11. A. V. Pogorelov, *Differential Geometry* (P Noordhoff N. V., Groningen, 1956).
 12. S. Venkataramani, T. Witten, E. Kramer, and R. Geroch, *Journal of Mathematical Physics* **41**, 5107 (2000).